Photocatalytic Properties of Graphdiyne and Graphene Modified TiO_2: From Theory to Experiment

Nailiang Yang,[†,∥,¶] Yuanyuan Liu,[†,¶] Hao Wen,[†] Zhiyong Tang,[‡] Huijun Zhao,[§] Yuliang Li,[⊥] and Dan Wang[†,*]

[†]State Key Laboratory of Multiphase Complex Systems, Institute of Process Engineering, Chinese Academy of Sciences, Beijing 100190, People's Republic of China, [‡]National Center for Nanoscience and Technology, Beijing, People's Republic of China, [§]Centre for Clean Environment and Energy, Gold Coast Campus, Griffith University, Queensland 4222, Australia, [⊥]Key Laboratory of Organic Solids, Beijing National Laboratory for Molecular Sciences, Institute of Chemistry, Chinese Academy of Sciences, Beijing 100190, People's Republic of China, and [∥]University of Chinese Academy of Sciences, Beijing 100049, People's Republic of China. [¶]These authors contributed equally to this work.

ABSTRACT The chemical structure and electronic properties of two-dimensional (2D) carbon-supported TiO_2, TiO_2—graphdiyne, and TiO_2—graphene composites have been studied by first-principles density functional theory. Calculation results show that TiO_2(001)—graphdiyne composites possess superior charge separation and oxidation properties, having the longest lifetimes of photoexcited carriers among all of the 2D composites containing TiO_2 of different facets. Our experimental results further proved that TiO_2(001)—graphdiyne composites could be a promising photocatalyst. For photocatalytic degradation of methylene blue, the rate constant of the TiO_2(001)—graphdiyne composite is 1.63 ± 0.15 times that of the pure TiO_2(001) and 1.27 ± 0.12 times that of the TiO_2(001)—graphene composite.

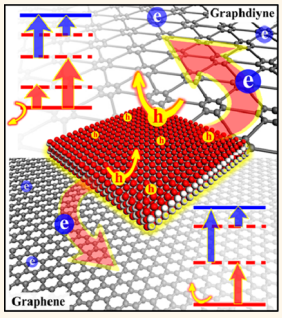

KEYWORDS: graphdiyne · graphene · TiO_2 · composite · crystal facet · DFT calculation · photocatalysis

Heterogeneous photocatalytic oxidation of organic compounds by titanium dioxide (TiO_2) has received much attention as a promising technology for pollution remediation due to strong UV light absorption, strong oxidation property, and excellent photostability of TiO_2. The efficiency of the photocatalytic process is measured by quantum yield (ϕ), which is defined as the number of events occurring per photon absorbed.[1] In an ideal system, ϕ is proportional to a simple relationship:

$$\phi \propto k_{CT}/(k_{CT} + k_R)$$

where k_{CT} is the rate of the charge transfer processes and k_R indicates the electron—hole recombination rate (both bulk and surface). The above equation reveals that preventing the electron—hole recombination of TiO_2 under illumination would be critical for improvement of the quantum yield, and a plausible way is to combine the semiconductor with some electron acceptors.[2] Among them, graphene (GR) has been confirmed to be a good candidate to form the composites with TiO_2 as the photocatalyst.[3]

Since isolated in 2004,[4] graphene had captured the attention of scientists because it is one of the thinnest and strongest materials in the world. Furthermore, GR is highly transparent, possesses high electrical and thermal conductivity, and has a large specific surface area.[5−7] Owning to these superior properties, GR and its composites have been extensively investigated for a variety of applications including supercapacitors,[8−10] fuel cells,[11] batteries,[12] catalysis,[13,14] photovoltaics,[15,16] chemical and biosensors,[17−21] photonics,[22] and optoelectronics.[23]

Graphdiyne (GD), another 2D carbon allotrope that contains both sp and sp^2 carbon atoms, was predicted by Baughman in 1997.[24] Li and co-workers successfully synthesized large-area graphdiyne films on the surface of copper *via* a cross-coupling reaction using hexaethynylbenzene precursors in 2010.[25] The resultant GD showed semiconducting property with a measured conductivity of 2.516×10^{-4} S/m and was predicted to be the most stable structure among various diacetylenic non-natural carbon allotropes because of the dialkyne between the benzene rings.[26] Also, Malko

* Address correspondence to danwang@mail.ipe.ac.cn.

Received for review November 14, 2012 and accepted January 25, 2013.

Published online January 27, 2013
10.1021/nn305288z

predicted that some GD allotropes, which do not have hexagonal symmetry and two self-doped nonequivalent distorted Dirac cones, could possess electronic properties superior to that of graphene.[27] However, these reports are purely based on the theoretical prediction without sufficient experimental support.

Density functional theory (DFT) calculations predicted that graphdiyne is a narrow direct band gap material. Remarkably, the calculated intrinsic charge mobility of a graphdiyne sheet is up to 10^5 $cm^2 V^{-1} s^{-1}$ at room temperature in some allotropes,[28] which is similar to the value of graphene.[29,30] Such a high change mobility suggests that GD should have excellent electron transport property, which may be utilized in the composites to improve the photocatalytic performance of TiO_2. This hypothesis was partially confirmed by our previous work that the P25−GD nanocomposite gave a good catalysis performance.[31] Nevertheless, understanding the charge transfer mechanism at the interface of TiO_2 and graphdiyne was found to be difficult due to the complicated phases and facets of the loaded P25 samples.

In this article, DFT calculation is employed to investigate charge transfer actions between 2D carbon materials and anatase TiO_2 of different crystal facets. The surface free energies of anatase TiO_2 crystals with different facets can vary significantly[32,33] because of the distinctive surface atomic arrangements. In general, {001} and {110} facets of anatase TiO_2 have high surface energy[34,35] compared with the most commonly obtained {101} facets.[36] Herein, we chose the aforementioned three anatase TiO_2 facets to composite with GD and GR, respectively. For DFT calculation, the supercells of six composites were built and geometrically optimized. The results of calculation and experiment show that the TiO_2(001)−GD has the most effective charge separation capacity, the most abundant impurity levels, and the highest oxidation ability, exhibiting an oxidative degradation rate constant of 1.63 times that of pure TiO_2(001) and 1.27 times that of TiO_2(001)−GR composites.

RESULTS AND DISCUSSION

The density functional theory (DFT) employing a Dmol^3 code was used to calculate the electronic structure of different types of 2D TiO_2−carbon composite materials. The supercells of six composites (defined as TiO_2(001)−GD, TiO_2(101)−GD, TiO_2(110)−GD, TiO_2(001)−GR, TiO_2(101)−GR, and TiO_2(110)−GR) were built, and the optimized structures are shown in Figure S1 of the Supporting Information. For TiO_2(101)−GR and TiO_2(110)−GR composites, the equilibrium distances between graphene and TiO_2 are so large that even the nearest C atoms were as far as 3.185 and 3.34 Å to the TiO_2 planes, indicating the weak interaction between GR and the TiO_2 surface. For TiO_2(101)−GD, TiO_2(110)−GD, and TiO_2(001)−GR composites, thanks to the strong adsorption between carbon atoms and the TiO_2 support,[37] numbers of new C−O bonds are formed from O in TiO_2 and atop C in GD or GR. Especially for the TiO_2(001)−GD composite, besides C−O bonds, the new Ti−C bonds are also obtained. Those new bonds demonstrated the chemisorbed situation between TiO_2 and GD or GR.[38] In the case of GR, only chemical bond formation with {001} facets could occur; however, more active GD could be chemisorbed with every facets of TiO_2, giving rise to strong electron hybridization. The calculated results also indicate that the shortest C−O bond (*ca.* 1.354−1.433 Å) is formed in the TiO_2(001)−GD system among the entire composites, suggesting the strongest C−O bond formation compared to the other five composites (Table S1).

In detail, the formation of C−O−Ti and C−Ti bonds can be observed by the electron density differences (Figure 1a,b). For the TiO_2(001)−GR composite, the C−O σ bond is formed by O and atop C atoms, which plays a bridge role in the charge transfer at the interface between TiO_2 and GR. Moreover, for the TiO_2(001)−GD composite, besides the C−O bond, another Ti−C π bond is also formed (top right pictures in Figure 1a). This particular bond would make TiO_2 anchor to the GD layer tightly, which is beneficial for the charge transfer. The bonding formation can also be observed from the experimental results of X-ray photoelectron spectroscopy (XPS) and Fourier transform infrared (FTIR) spectra in the following discussion (Figure 2d and Figure S4).

To further demonstrate the charge transfer ability, we calculated the Mulliken charge for the surface of TiO_2(001)−GD and TiO_2(001)−GR (Figure 1c). It can be seen that the GD or GR surface has a positive Mulliken charge, forming a large opposite interface dipole at the interface,[39,40] leading to a strong built-in electric field throughout the superlattice. In this case, with light excitation, the tendency of electron transport to carbon would be high, prolonging the holes' lifetime at the valence band of TiO_2. This feature suppresses the charge recombination and thus improves the photocatalytic activity. Since the magnitude of charge accumulation in GD is larger than the GR surface, stronger electrons' capture ability of TiO_2(001)−GD composites could be expected compared to TiO_2(001)−GR composites.

Because the {001} facets possess the strongest bond formation with carbon materials, we chose TiO_2 with exposed {001} facets in the following experiments to verify the calculation results. In a typical experiment, the anatase TiO_2 nanosheets with exposed {001} facets were synthesized by a hydrothermal method according to Lou's report.[41] Scanning electron microscopy (SEM) images confirm that the sample contains very large carpet-like structures with a side length of several micrometers and a thickness of *ca.* 30 nm (Figure S3a). These 2D structures are formed *via* the lateral aggregation of smaller TiO_2 nanosheets. The

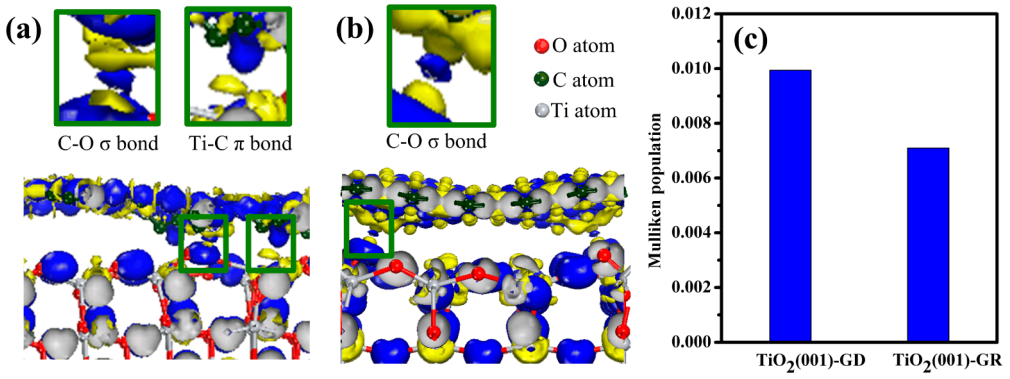

Figure 1. Plots of electron density difference at the composites interfaces: (a) TiO_2(001)−GD, (b) TiO_2(001)−GR. Isosurface values for electron density difference plots are −0.08 and 0.08 e/Å^3, where the accumulation and depletion of electrons are represented in blue and yellow, respectively. (c) Mulliken charge of GD or GR surface in the composites.

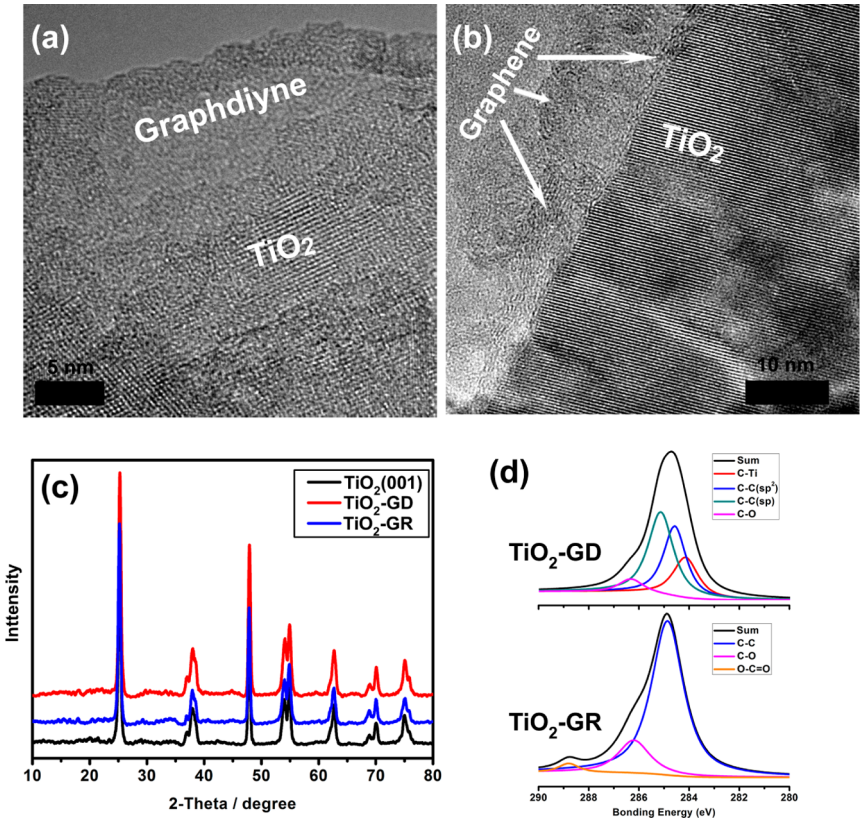

Figure 2. HR-TEM images of (a) TiO_2(001)−GD and (b) TiO_2(001)−GR composites. (c) XRD pattern of different materials. (d) C 1s XPS spectra of TiO_2(001)−GD and TiO_2(001)−GR.

transmission electron microscopy (TEM) images further confirm the morphology characteristics of nanosheets, and the highly symmetric selected area electron diffraction (SAED) pattern can be indexed as [001] zone (Figure S3b,d).[42] In addition, the high-resolution TEM (HR-TEM) image clearly shows the continuous (100) atomic planes with a lattice spacing of *ca.* 3.7 Å, corresponding to the {100} planes of anatase TiO_2 single crystals (Figure S3c).[43] The X-ray diffraction (XRD) patterns of the products are presented in Figure 2c. All of the identified peaks can be unambiguously assigned to anatase TiO_2 (JCPDS card no. 21-1272; space group $I4_1/amd$; a_0 = 3.7852 Å, c_0 = 9.5139 Å). The Raman spectrum also shows the typical peaks of anatase phase without any rutile phase, and the typical vibration of GD and GR can also be distinguished from their composites (Figure S4).

A series of TiO_2(001)−GD and TiO_2(001)−GR composites with different ratios of GD or GR to TiO_2 are obtained by a simple hydrothermal treatment of the 2D TiO_2 and 2D GD or 2D GR in a mixture of ethanol and water. No typical XRD diffraction peaks of GR and GD could be observed from the composite samples (Figure 2c), which is reasonable because the sharp

peak of anatase TiO_2 shielded the main characteristic peak of GR and GD.[31] Figure 2a,b shows the HR-TEM images of the TiO_2(001)−GD and TiO_2(001)−GR composites, respectively. The revealed lattice fringes are assigned to the TiO_2 nanosheets, and the amorphous morphology is attributed to graphdiyne (Figure 2a). Also, the few curving fringes correspond to the few-layer graphene (Figure 2b). Figure 2a,b indicates a perfect connection between TiO_2 and 2D carbon sheets. It should be noted that such connections are not only the physical attachment but also the chemical bonding. The high-resolution C 1s XPS spectra of the composites (Figure 2d) reveal that the carbon materials are successfully bound with TiO_2. The C 1s XPS spectrum of TiO_2(001)−GR indicates the presence of three types of carbon bonds at 284.9, 286.4, and 288.8 eV that can be assigned to a C 1s orbital of C−C, C−O, and O−C═O, respectively.[44] Notably, an additional peak at 284.1 eV is discerned from the spectrum of TiO_2(001)−GD, corresponding to the presence of a Ti−C bond in the TiO_2(001)−GD sample.[45] Besides, the C−C bond could be fitted to C−C(sp) and C−C(sp^2) located at 285.2 and 284.5 eV, respectively, which is ascribed to the benzene rings' similar structure by diacetylenic linkages in GD.[25] These results are also supported by the DFT calculation results (Figure 1).

The C−O−Ti bond formation is also explored by FTIR spectroscopy (Figure S5). For both TiO_2(001)−GD and TiO_2(001)−GR, the broad absorption at *ca.* 500 cm^{-1} represents the Ti−O−Ti stretching vibrations,[46] while the new bands near 1150 cm^{-1} are assigned to the Ti−O−C stretching modes.[47] The DFT simulation also matches the characterization results perfectly (Figure 1a,b).

The above theoretical calculations and structural characterizations suggest that TiO_2(001)−carbon bonds have superior charge transport properties that would enhance the photocatalytic activity. The photocatalytic degradation of methylene blue (MB) is used as a model system to validate this prediction (Figure 3). The normalized temporal concentration change (C/C_0) of MB during the photocatalytic degradation experiment is found to be proportional to the normalized maximum absorbance (A/A_0), which is derived from the changes in the dye's absorption profile (λ = 663 nm) at a given time interval.

It is found that the degradation efficiency is dependent on GD or GR loading in the composite (Table 1). According to a previous report,[48] the decomposition of dye could be assigned to a pseudo-first-order kinetics reaction with a simplified Langmuir−Hinshelwood model when C_0 is low.[49] That is

$$\ln(C_0/C) = kt$$

where k is the apparent first-order rate constant. For the pure TiO_2(001), the obtained k value is estimated to be 0.0152 min^{-1}. While for a TiO_2(001)−GD composite of 0.4 wt % GD, k is highest and up to 0.0247 min^{-1},

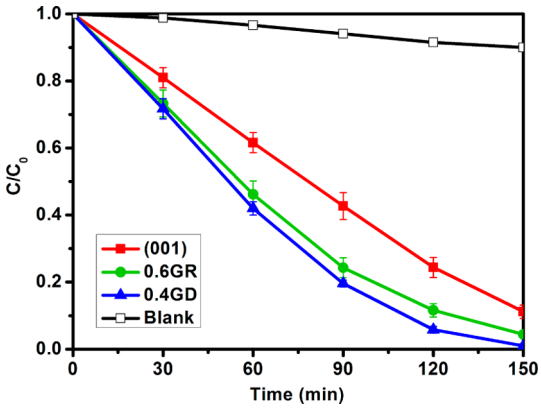

Figure 3. Photocatalytic degradation of MB over TiO_2(001), TiO_2(001)−GD, TiO_2(001)−GR composites, and the blank experiment (without any photocatalyst).

TABLE 1. Photocatalytic Degradation Reaction Kinetics over TiO_2 Nanosheets with Different GD and GR Loading Content

loading (wt %)		0	0.2	0.4	0.6	0.8
$k/10^{-2}$ min^{-1}	GD	1.52	2.24	2.47	2.34	2.30
	GR	1.52	1.58	1.66	1.95	1.65

which is 1.62 times that obtained from the pure TiO_2-(001). For the TiO_2(001)−GR composites, a weight ratio of 0.6% GR loading gives the highest rate constant of 0.0195 min^{-1}, 1.28 times that of pure TiO_2(001). For all of the cases investigated, the 2D carbon-based TiO_2 composite shows higher photocatalytic efficiencies than that of the pure TiO_2 nanosheets, which should be attributed to the synergetic charge transfer effect of the composites. The effect of GD and GR loading on the performance of the resultant composites would be explained based on the balance between the benefit of synergetic charge transport and reduced light utilization efficiency. Because both GD and GR of strong light absorbance reduce the light utilization efficiency, excess amount of GD or GR loading would overwhelm the benefit of synergetic charge transport, resulting in a decreased efficiency. The lower GD loading to reach such a critical point is because the GD is relatively thicker and difficult to be dispersed than that of GR.[25] Meanwhile, considering that all three samples have similar specific surface areas (Figure S6), the higher dye absorption amount of the TiO_2(001)−GD and TiO_2(001)−GR composites is attributed to the $\pi-\pi$ stacking between dye molecules and 2D carbon sheets. Interestingly, in comparison of TiO_2(001)−GD and TiO_2(001)−GR composites, the GR composite shows the better adsorptivity because of the large π-conjugation structures (Figure S6), whereas the GD composite performs better in the following photodegradation process, which should be attributed to its electronic properties. In detail, the excellent photocatalytic activity of the TiO_2(001)−GD composites could be ascribed to the following reasons.

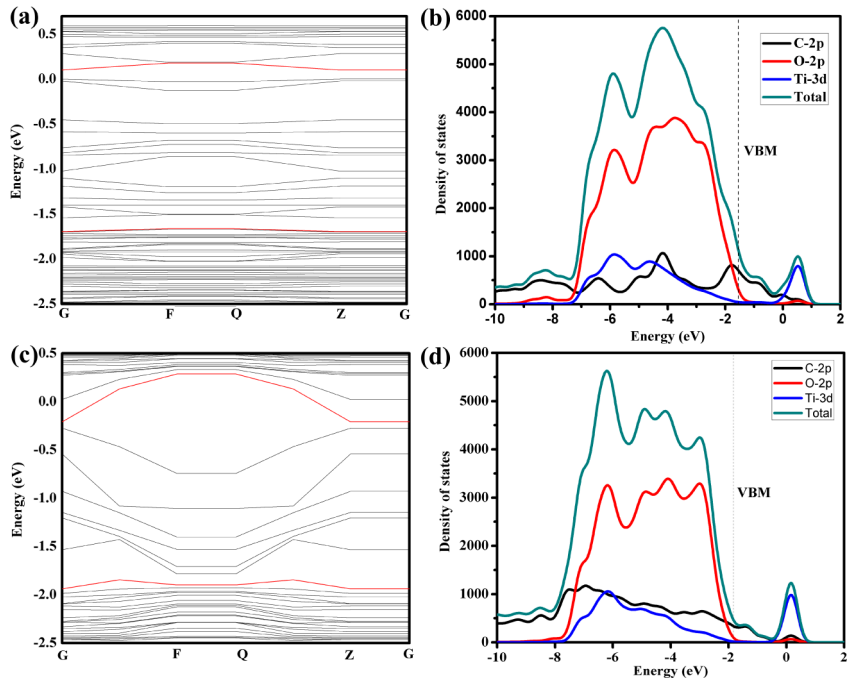

Figure 4. Band structure and partial density of states (PDOS) for the composites. Band structures of (a) TiO_2(001)−GD and (b) TiO_2(001)−GR. PDOS of (b) TiO_2(001)−GD and (d) TiO_2(001)−GR. The Fermi level is set to zero. The red lines represent the CBM and VBM position of the composites.

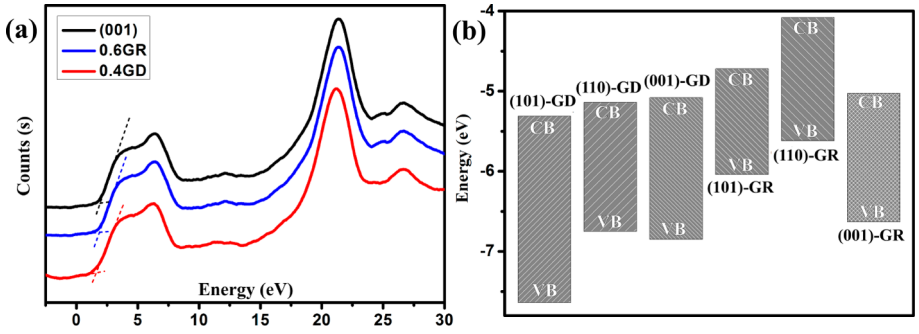

Figure 5. (a) XPS VB spectra and (b) CB, VB position of different composites. TiO_2−GD composites always have lower VB positions with respect to TiO_2−GR composites.

TiO_2−GD Composites Possess Improved Charge Separation Ability. In the TiO_2−carbon composite materials, the photogenerated electrons from TiO_2 can be captured by the π-conjugated structure of carbon *via* a percolation mechanism. Hence, both GD and GR act as the electron acceptors in the TiO_2−carbon system, effectively suppressing the charge recombination and leaving more holes to form reactive species that promote the degradation of dyes. On the basis of analysis with DFT method and XPS (Figures 1 and 2), the GD has the strongest bonding and the largest dipole with the {001} facet of TiO_2, which is able to promote the charge separation, retard the recombination, and increase the photocatalytic ability.

TiO_2−GD Composites Possess Abundant Impurity Levels. To gain insight into the electronic structure of composites, the band structures and partial density of states (PDOS) of the six TiO_2−carbon composites are illustrated in Figure 4 and Figure S2.

Figure S2 shows that there are no isolated energy levels in the band gap of TiO_2(101)−GR or TiO_2(110)−GR composites. While due to the strong hybridization and bond formation, many isolated energy levels localized between the valence band maximum (VBM) and conduction band minimum (CBM) can be discerned for both TiO_2(001)−GR and TiO_2(001)−GD composites (Figure 4 and Figure S2).[50] According to the electron energy band structure theory, the impurity levels near the VBM belong to p-type doping, while those close to the CBM are considered as n-type doping. Attributing the hole and electron as the donor for the p-type and n-type doping, respectively, we can deduce from Figures 4 and S1 that both positive and negative charges are introduced into the composites. Carbon atoms are reported to show

TABLE 2. Calculated Fermi Energy and VB and CB Positions of the TiO_2(001)−GD or TiO_2(001)−GR Composites

	E_{Fermi} (eV)	$\Delta E_{calcd/exptl}$ (eV)	VB[a] (eV)	CB (eV)
TiO_2(001)−GD	−5.19	1.66/1.62	−6.85	−5.08
TiO_2(001)−GR	−4.82	1.81/1.88	−6.63	−5.03

[a] VB = $E_{Fermi} - E_{calcd/exptl}$; E_{exptl} is the value between VB and Fermi level from the XPS data.

different valences of the (−2, +4) prices[51,52] when GD or GR is mixed with TiO_2. In this case, the impurity level is independent and it is not recombined, resulting in the electron transfer from VBM to an isolated energy level or from an isolated energy level to CBM more easily. Meanwhile, with these isolated levels, the electrons are more difficult to fall back from CB to VBM, which retards the corresponding recombination.[53] The electronic excitation energy from the occupied isolated energy levels to the CBM is also smaller than the energy from the VBM to CBM, which makes the electrons excited more easily. Here, we conclude that, because GD introduces the impurity levels to TiO_2 more easily, while GR can only react with the TiO_2(001) facet, GD can be considered as a better material for property modification compared with GR. Furthermore, the (001) facet of TiO_2 is the active facet so that it is easier to be modified by GR. Also, the TiO_2(001)−GD composites have the most impurity levels among all of the composites (Figures S2 and Figure 4), so there are more donor and acceptor impurity levels for the electrons and the recombination will be prevented more efficiently.

It is noted that, for all TiO_2−GD composites, the valence band is formed by the hybrid of C 2p and O 2p orbitals. The shallow impurity level that is close to the VBM of the composites is obtained by the O 2p orbital and C 2p orbital, while the deep impurity level is mainly constituted by the C 2p orbital. As a comparison, for the TiO_2(001)−GR composites, the valence band is also formed by the hybrid of C 2p and O 2p orbitals, but both the shallow and deep impurity states only originate from C 2p electrons (Figure 4 and Figure S2). In both TiO_2(001)−GD and TiO_2(001)−GR composites, continuum states near the VBM are formed rather than an isolated state, which can benefit enhancing the lifetime of the photoexcited carriers.[54] The magnitude of PDOS of the continuum states of TiO_2(001)−GD is stronger than that of TiO_2(001)−GR, revealing that the lifetime of the photoexcited carriers in TiO_2(001)−GD is longer than that in TiO_2(001)−GR.

TiO_2−GD Composites Possess Higher Oxidation Ability. X-ray photoelectron valence band spectra (Figure 5a) show that the VB maxima of all three materials have some differences. The VB values of pure TiO_2(001) are *ca.* 1.95 eV lower than the Fermi level, which is consistent with the former report.[55,56] For the TiO_2(001)−GD and TiO_2(001)−GR, the VB values are *ca.* 1.62 and 1.88 eV lower than their Fermi levels, respectively, which are similar to the simulation results (Table 2). We also identify the valence band position of the composites by analyzing their band structure and the partial density of states in Figure 4, Figure 5, and Figure S2. The calculation results based on Figure 4 and Figure 5 show that, accompanying the shift of the Fermi level, the valence band positions for the TiO_2(101)−GD, TiO_2(110)−GD, TiO_2(001)−GD, TiO_2(101)−GR, TiO_2(110)−GR, and TiO_2(001)−GR composites are −7.64, −6.75, −6.85, −6.04, −5.62, and −6.63 eV, respectively. It proves that the TiO_2−GD composites always have the lower VB positions with respect to the corresponding TiO_2−GR composites. The more negative VB values would have higher oxidation ability.[57] In other words, compared to TiO_2−GR composites, TiO_2−GD composites always show higher oxidation ability, which leads to a higher photodegradation performance.

CONCLUSION

In conclusion, the chemical structure and electronic properties of TiO_2−GD and TiO_2−GR composites with different TiO_2 facets are calculated by first-principles density functional theory. The results disclose that the TiO_2(001)−GD composite exhibits the most outstanding performance in rich electronic structure, charge separation, and the oxidation ability compared with pure TiO_2(001) or TiO_2(001)−GR composite, which makes it an excellent photocatalyst candidate with high efficiency. Our experiment further confirms the theoretical prediction that the TiO_2(001)−GD composite shows the highest photocatalysis performance compared with other 2D carbon-based TiO_2 composites, even including TiO_2(001)−GR. As a result, we can expect that graphdiyne will become a superb competitor among the different types of 2D carbon materials in the applications of photocatalysis and photovoltaics.

METHODS

Reagents. Titanium isopropoxide was purchased from J&K Company. HF (>48%) was purchased from Aladdin Reagent Company. Flake graphite with 4 μm average particle diameter was purchased from Qingdao Tianhe Graphite Co. Ltd., China. Unless otherwise specified, MB and other reagents and materials were obtained commercially from the Beijing Chemical Reagent Plant (Beijing, China) and used as received without further purification. The experiments were carried out at room temperature and humidity.

Synthesis of TiO_2 with (001) Facets Exposed. TiO_2 was synthesized by following Lou's method.[41] Briefly, 3 mL of 48% HF was slowly added into 10 mL of titanium isopropoxide in a 100 mL Teflon-lined stainless steel autoclave under mild stirring, and then it was heated at 180 °C for 24 h. After being cooled naturally to room temperature, the white product was harvested and washed thoroughly with DI water and ethanol by filtration, which was then dried at 60 °C overnight.

Synthesis of Graphene Oxide (GO). GO was synthesized from flake graphite by a modified Hummer's method.[15] Briefly, graphite powder (5 g) and $NaNO_3$ (3.75 g) were placed in a flask. Then, concentrated H_2SO_4 (375 mL) was added slowly with stirring in an ice–water bath. $KMnO_4$ (22.5 g) was added gradually under stirring over 1 h, and the mixture was kept stirring for another 2 h. After stirring vigorously for 5 days at room temperature, the mixture was stirred at 35 °C for 2 h and then diluted with 5 wt % H_2SO_4 aqueous solution (700 mL) over 1 h. After being stirred at 98 °C for 2 h, when the temperature was reduced to 60 °C, 30 wt % H_2O_2 (30 mL) was added and the mixture was stirred for 2 h at room temperature. The mixture was centrifuged and washed with an aqueous solution of 3 wt % H_2SO_4/0.5 wt % H_2O_2 (2 L) 15 times. Then the precipitate was washed with 3 wt % HCl (2 L) aqueous solution by a similar procedure and once using H_2O (2 L). After adding another 2 L of deionized water and dispersing the solid using vigorous stirring and bath ultrasonication for 30 min, the final water solution was treated with a weak basic ion-exchange resin to remove the remaining HCl. The final solution was concentrated to 7.5 mg mL^{-1}.

Synthesis of GD[25]. GD was synthesized on the surface of copper *via* a cross-coupling reaction using hexaethynylbenzene as the precursors. In brief, the monomer of hexaethynylbenzene was synthesized in good yield (62%) by addition of tetrabutylammonium fluoride (TBAF) to a THF solution of hexakis-[(trimethylsilyl)ethynyl]benzene for 10 min at 8 °C. The GD was successfully grown on the surface of copper foil in the presence of pyridine by a cross-coupling reaction of the monomer of hexaethynylbenzene for 72 h at 60 °C under a nitrogen atmosphere. In the process of forming GD, the copper foil was not only the catalyst for the cross-coupling reaction but also the substrate for the growing GD film.

Synthesis of Composite Photocatalysts. The TiO_2(001)–GD and TiO_2(001)–GR composites were obtained *via* a hydrothermal method. Briefly, GD or GO was dissolved in a solution of distilled H_2O (20 mL) and ethanol (40 mL) by ultrasonic treatment for 1 h, and a proper weight of TiO_2 was added to the obtained solution which was stirred for another 2 h to achieve a homogeneous suspension. The suspension was then placed in a 100 mL Teflon-sealed autoclave and maintained at 120 °C for 3 h to achieve the composite of TiO_2 and carbon. Finally, the resulting composite was recovered by filtration, rinsed with ethanol several times, and dried at room temperature. On the basis of the XPS data (Figure S7), the content of oxygen in GO samples was about 33%, while after the reduction, there was only 8% oxygen left in the sample of the reduced graphene oxide. If we assumed that the amount of C element could not be lost during the reduction process, the weight loss of graphene oxide after the reduction was estimated to be around 27% based on the simple calculation. Note: the graphene amount in the composite was calculated on the reduced graphene oxide (0.6% loading represented that the composite contained 0.6 mg of reduced graphene oxide and 99.4 mg of TiO_2).

Photocatalytic Experiments. Photodegradation of MB was observed by using UV–vis absorption spectroscopy. In a typical process, 30 mg of photocatalyst was added into an aqueous solution of MB (0.01 g L^{-1}, 2.7 × 10^{-5} M, 40 mL) placed in a 50 mL cylindrical quartz vessel, ultrasonic dispersion before being stirred in the dark for 30 min. At given time intervals, the photoreacted solution was analyzed by recording variations of the absorption band maximum (663 nm) in the UV–vis spectra of MB. Under ambient conditions, 300 K recirculated water, and stirring, the photoreaction vessel was exposed to the AM 1.5 solar simulator illumination (Xe lamp, 100 mW/cm^2).

Characterization. The XRD patterns were obtained by using an X'Pert PRO MDP instrument with Cu Kα radiation (λ = 1.5405 Å) at 30 mA and 40 kV. SEM images were obtained using a JEOL JSM-6700F scanning electron microscope at 3.0 kV. TEM and SAED images were obtained on a JEOL-1011 at 100 kV. HR-TEM images were obtained on an FEI Tecnai F20 instrument at an acceleration voltage of 200 kV. FTIR spectra were recorded on a Bruker EQUINOX55 FTIR spectrophotometer. UV–vis spectra were recorded on a Hitachi model U-4100 spectrophotometer. XPS VB data were obtained with an ESCALab220i-XL electron spectrometer from VG Scientific using 300 W Al Kα radiation. The binding energies obtained in the XPS analysis were corrected with reference to C 1s (284.8 eV). Raman spectra were measured on a Renishaw-2000 Raman spectrometer at a resolution of 1 cm^{-1} by using an argon ion laser of the 514.5 nm line as the excitation source. The nitrogen adsorption and desorption isotherms at the temperature of liquid nitrogen (77 K) were measured on a Quantachrome Autosorb-1 sorption analyzer. Multipoint BET surface area was estimated at the relative pressure range from 0.05 to 0.2.

Computation Details. We performed DFT calculations using the Dmol[3] code with the generalized gradient approximation (GGA) and PW91. Double numerical plus polarization (DNP) with a real-space cutoff of 5.2 Å had been employed during the geometry optimization and single-point energy calculation. DFT semicore pseudopots were implemented for relativistic effects, which replaced core electrons by effective potentials of Ti elements; all-electron was used as the core treatment for O and C elements. The maximum energy change convergence threshold for self-consistent field (SCF) was 1 × 10^{-6} Ha/atom; atomic relaxation was carried out until all components of the residual forces were less than 0.002 Ha/Å, and the maximum displacement was within 0.005 Å. Monkhorst-Pack *k*-point mesh was used for geometry optimization and electronic property calculations.

Because of the different lattice parameters of GD, GR, and TiO_2, we chose different supercells to make sure that the mismatch of the TiO_2–GR or GD surfaces was less than 5.31%. A vacuum layer larger than 15 Å was used to avoid the spurious interactions between two adjacent layers, and the optimized structure of the composite is shown in Figure S1.

Conflict of Interest: The authors declare no competing financial interest.

Acknowledgment. We are grateful for financial support from the National Natural Science Foundation of China (Nos. 21031005, 21203201, 91122014, 51172235, 20971125, and 21006116), the Foundation for State Key Laboratory of Multiphase Complex Systems (No. MPCS-2012-A-08). We thank Prof. W. Huang at the Institute of Process Engineering, Chinese Academy of Sciences, for his help with the calculation. Calculations were carried out at the Shanghai Supercomputer Center.

Supporting Information Available: Detailed experimental procedures and additional figures. This material is available free of charge *via* the Internet at http://pubs.acs.org.

REFERENCES AND NOTES

1. Linsebigler, A. L.; Lu, G.; Yates, J. T. Photocatalysis on TiO_2 Surfaces: Principles, Mechanisms, and Selected Results. *Chem. Rev.* **1995**, *95*, 735–758.
2. Pelaez, M.; Nolan, N. T.; Pillai, S. C.; Seery, M. K.; Falaras, P.; Kontos, A. G.; Dunlop, P. S. M.; Hamilton, J. W. J.; Byrne, J. A.; O'Shea, K.; *et al.* A Review on the Visible Light Active Titanium Dioxide Photocatalysts for Environmental Applications. *Appl. Catal., B* **2012**, *125*, 331–349.
3. Zhang, H.; Lv, X.; Li, Y.; Wang, Y.; Li, J. P25-Graphene Composite as a High Performance Photocatalyst. *ACS Nano* **2009**, *4*, 380–386.
4. Novoselov, K. S.; Geim, A. K.; Morozov, S. V.; Jiang, D.; Zhang, Y.; Dubonos, S. V.; Grigorieva, I. V.; Firsov, A. A. Electric Field Effect in Atomically Thin Carbon Films. *Science* **2004**, *306*, 666–669.
5. Wee, A. T. S. Graphene: The Game Changer? *ACS Nano* **2012**, *6*, 5739–5741.
6. Huang, X.; Qi, X.; Boey, F.; Zhang, H. Graphene-Based Composites. *Chem. Soc. Rev.* **2012**, *41*, 666–686.
7. Huang, X.; Yin, Z.; Wu, S.; Qi, X.; He, Q.; Zhang, Q.; Yan, Q.; Boey, F.; Zhang, H. Graphene-Based Materials: Synthesis, Characterization, Properties, and Applications. *Small* **2011**, *7*, 1876–1902.
8. Wu, Q.; Xu, Y. X.; Yao, Z. Y.; Liu, A. R.; Shi, G. Q. Supercapacitors Based on Flexible Graphene/Polyaniline Nanofiber Composite Films. *ACS Nano* **2010**, *4*, 1963–1970.
9. Huang, X.; Zeng, Z.; Fan, Z.; Liu, J.; Zhang, H. Graphene-Based Electrodes. *Adv. Mater.* **2012**, *24*, 5979–6004.

10. Cao, X.; Shi, Y.; Shi, W.; Lu, G.; Huang, X.; Yan, Q.; Zhang, Q.; Zhang, H. Preparation of Novel 3D Graphene Networks for Supercapacitor Applications. *Small* **2011**, *7*, 3163–3168.
11. Qu, L.; Liu, Y.; Baek, J.-B.; Dai, L. Nitrogen-Doped Graphene as Efficient Metal-Free Electrocatalyst for Oxygen Reduction in Fuel Cells. *ACS Nano* **2010**, *4*, 1321–1326.
12. Liu, H.; Wang, G. X.; Liu, J.; Qiao, S. Z.; Ahn, H. J. Highly Ordered Mesoporous NiO Anode Material for Lithium Ion Batteries with an Excellent Electrochemical Performance. *J. Mater. Chem.* **2011**, *21*, 3046–3052.
13. Huang, C.; Li, C.; Shi, G. Graphene Based Catalysts. *Energy Environ. Sci.* **2012**, *5*, 8848–8868.
14. Wu, S.; He, Q.; Zhou, C.; Qi, X.; Huang, X.; Yin, Z.; Yang, Y.; Zhang, H. Synthesis of Fe_3O_4 and Pt Nanoparticles on Reduced Graphene Oxide and Their Use as a Recyclable Catalyst. *Nanoscale* **2012**, *4*, 2478–2483.
15. Yang, N.; Zhai, J.; Wang, D.; Chen, Y.; Jiang, L. Two-Dimensional Graphene Bridges Enhanced Photoinduced Charge Transport in Dye-Sensitized Solar Cells. *ACS Nano* **2010**, *4*, 887–894.
16. Chen, C.; Cai, W.; Long, M.; Zhou, B.; Wu, Y.; Wu, D.; Feng, Y. Synthesis of Visible-Light Responsive Graphene Oxide/TiO_2 Composites with P/N Heterojunction. *ACS Nano* **2010**, *4*, 6425–6432.
17. He, Q. Y.; Zeng, Z. Y.; Yin, Z. Y.; Li, H.; Wu, S. X.; Huang, X.; Zhang, H. Fabrication of Flexible MoS_2 Thin-Film Transistor Arrays for Practical Gas-Sensing Applications. *Small* **2012**, *8*, 2994–2999.
18. He, Q.; Wu, S.; Gao, S.; Cao, X.; Yin, Z.; Li, H.; Chen, P.; Zhang, H. Transparent, Flexible, All-Reduced Graphene Oxide Thin Film Transistors. *ACS Nano* **2011**, *5*, 5038–5044.
19. Sudibya, H. G.; He, Q.; Zhang, H.; Chen, P. Electrical Detection of Metal Ions Using Field-Effect Transistors Based on Micropatterned Reduced Graphene Oxide Films. *ACS Nano* **2011**, *5*, 1990–1994.
20. Cao, X.; He, Q.; Shi, W.; Li, B.; Zeng, Z.; Shi, Y.; Yan, Q.; Zhang, H. Graphene Oxide as a Carbon Source for Controlled Growth of Carbon Nanowires. *Small* **2011**, *7*, 1199–1202.
21. He, Q.; Wu, S.; Yin, Z.; Zhang, H. Graphene-Based Electronic Sensors. *Chem. Sci.* **2012**, *3*, 1764–1772.
22. Bao, Q.; Loh, K. P. Graphene Photonics, Plasmonics, and Broadband Optoelectronic Devices. *ACS Nano* **2012**, *6*, 3677–3694.
23. Sun, Z. P.; Hasan, T.; Torrisi, F.; Popa, D.; Privitera, G.; Wang, F. Q.; Bonaccorso, F.; Basko, D. M.; Ferrari, A. C. Graphene Mode-Locked Ultrafast Laser. *ACS Nano* **2010**, *4*, 803–810.
24. Haley, M. M.; Brand, S. C.; Pak, J. J. Carbon Networks Based on Dehydrobenzoannulenes: Synthesis of Graphdiyne Substructures. *Angew. Chem., Int. Ed. Engl.* **1997**, *36*, 836–838.
25. Li, G.; Li, Y.; Liu, H.; Guo, Y.; Li, Y.; Zhu, D. Architecture of Graphdiyne Nanoscale Films. *Chem. Commun.* **2010**, *46*, 3256–3258.
26. Diederich, F. Carbon Scaffolding-Building Acetylenic All-Carbon and Carbon-Rich Compounds. *Nature* **1994**, *369*, 199–207.
27. Malko, D.; Neiss, C.; Vines, F.; Goerling, A. Competition for Graphene: Graphynes with Direction-Dependent Dirac Cones. *Phys. Rev. Lett.* **2012**, *108*, 086804.
28. Long, M.; Tang, L.; Wang, D.; Li, Y.; Shuai, Z. Electronic Structure and Carrier Mobility in Graphdiyne Sheet and Nanoribbons: Theoretical Predictions. *ACS Nano* **2011**, *5*, 2593–2600.
29. Berger, C.; Song, Z.; Li, X.; Wu, X.; Brown, N.; Naud, C.; Mayou, D.; Li, T.; Hass, J.; Marchenkov, A. N.; *et al.* Electronic Confinement and Coherence in Patterned Epitaxial Graphene. *Science* **2006**, *312*, 1191–1196.
30. Tan, Y. W.; Zhang, Y.; Bolotin, K.; Zhao, Y.; Adam, S.; Hwang, E. H.; Das Sarma, S.; Stormer, H. L.; Kim, P. Measurement of Scattering Rate and Minimum Conductivity in Graphene. *Phys. Rev. Lett.* **2007**, *99*, 246803.
31. Wang, S.; Yi, L.; Halpert, J. E.; Lai, X.; Liu, Y.; Cao, H.; Yu, R.; Wang, D.; Li, Y. A Novel and Highly Efficient Photocatalyst Based on P25-Graphdiyne Nanocomposite. *Small* **2012**, *8*, 265–271.
32. Lazzeri, M.; Vittadini, A.; Selloni, A. Structure and Energetic of Stoichiometric TiO_2 Anatase Surfaces. *Phys. Rev. B* **2001**, *63*, 155409.
33. Diebold, U. The Surface Science of Titanium Dioxide. *Surf. Sci. Rep.* **2003**, *48*, 53–229.
34. Yang, H. G.; Liu, G.; Qiao, S. Z.; Sun, C. H.; Jin, Y. G.; Smith, S. C.; Zou, J.; Cheng, H. M.; Lu, G. Q. Solvothermal Synthesis and Photoreactivity of Anatase TiO_2 Nanosheets with Dominant {001} Facets. *J. Am. Chem. Soc.* **2009**, *131*, 4078–4083.
35. Lazzeri, M.; Vittadini, A.; Selloni, A. Structure and Energetics of Stoichiometric TiO_2 Anatase Surfaces. *Phys. Rev. B* **2001**, *63*, 155409.
36. Yang, H. G.; Sun, C. H.; Qiao, S. Z.; Zou, J.; Liu, G.; Smith, S. C.; Cheng, H. M.; Lu, G. Q. Anatase TiO_2 Single Crystals with a Large Percentage of Reactive Facets. *Nature* **2008**, *453*, 638–641.
37. Jayasekera, T.; Xu, S.; Kim, K. W.; Nardelli, M. B. Electronic Properties of the Graphene/6H-SiC(000-1) Interface: A First-Principles Study. *Phys. Rev. B* **2011**, *84*, 035442.
38. Wang, Q. J.; Che, J. G. Origins of Distinctly Different Behaviors of Pd and Pt Contacts on Graphene. *Phys. Rev. Lett.* **2009**, *103*, 066802.
39. Wong, K.; Zeng, Q. H.; Yu, A. B. Electronic Structure of Metal (M = Au, Pt, Pd, or Ru) Bilayer Modified α-Fe_2O_3(0001) Surfaces. *J. Phys. Chem. C* **2011**, *115*, 4656–4663.
40. Khomyakov, P. A.; Giovannetti, G.; Rusu, P. C.; Brocks, G.; van den Brink, J.; Kelly, P. J. First-Principles Study of the Interaction and Charge Transfer between Graphene and Metals. *Phys. Rev. B* **2009**, *79*, 195429.
41. Chen, J. S.; Liu, J.; Qiao, S. Z.; Xu, R.; Lou, X. W. Formation of Large 2D Nanosheets *via* PVP-Assisted Assembly of Anatase TiO_2 Nanomosaics. *Chem. Commun.* **2011**, *47*, 10443–10445.
42. Liu, G.; Yang, H. G.; Wang, X.; Cheng, L.; Pan, J.; Lu, G. Q.; Cheng, H.-M. Visible Light Responsive Nitrogen Doped Anatase TiO_2 Sheets with Dominant {001} Facets Derived from TiN. *J. Am. Chem. Soc.* **2009**, *131*, 12868–12869.
43. Xiang, Q.; Yu, J.; Wang, W.; Jaroniec, M. Nitrogen Self-Doped Nanosized TiO_2 Sheets with Exposed {001} Facets for Enhanced Visible-Light Photocatalytic Activity. *Chem. Commun.* **2011**, *47*, 6906–6908.
44. Nethravathi, C.; Rajamathi, M. Chemically Modified Graphene Sheets Produced by the Solvothermal Reduction of Colloidal Dispersions of Graphite Oxide. *Carbon* **2008**, *46*, 1994–1998.
45. Akhavan, O.; Abdolahad, M.; Abdi, Y.; Mohajerzadeh, S. Synthesis of Titania/Carbon Nanotube Heterojunction Arrays for Photoinactivation of *E. coli* in Visible Light Irradiation. *Carbon* **2009**, *47*, 3280–3287.
46. Oliveira, C.; Gonçalves, L.; Almeida, B. G.; Tavares, C. J.; Carvalho, S.; Vaz, F.; Escobar-Galindo, R.; Henriques, M.; Susano, M.; Oliveira, R. XRD and FTIR Analysis of Ti-Si-C-ON Coatings for Biomedical Applications. *Surf. Coat. Technol.* **2008**, *203*, 490–494.
47. Pillai, S. C.; Periyat, P.; George, R.; McCormack, D. E.; Seery, M. K.; Hayden, H.; Colreavy, J.; Corr, D.; Hinder, S. J. Synthesis of High-Temperature Stable Anatase TiO_2 Photocatalyst. *J. Phys. Chem. C* **2007**, *111*, 1605–1611.
48. Sun, L.; Zhao, Z.; Zhou, Y.; Liu, L. Anatase TiO_2 Nanocrystals with Exposed {001} Facets on Graphene Sheets *via* Molecular Grafting for Enhanced Photocatalytic Activity. *Nanoscale* **2012**, *4*, 613–620.
49. Wang, X. H.; Li, J. G.; Kamiyama, H.; Moriyoshi, Y.; Ishigaki, T. Wavelength-Sensitive Photocatalytic Degradation of Methyl Orange in Aqueous Suspension over Iron(III)-Doped TiO_2 Nanopowders under UV and Visible Light Irradiation. *J. Phys. Chem. B* **2006**, *110*, 6804–6809.
50. Shi, W.-J.; Xiong, S.-J. *Ab Initio* Study of Water Adsorption on TiO_2-Terminated (100) Surface of $SrTiO_3$ with and without Cr Doping. *Surf. Sci.* **2010**, *604*, 1987–1995.
51. Zhu, W.; Qiu, X.; Iancu, V.; Chen, X.-Q.; Pan, H.; Wang, W.; Dimitrijevic, N. M.; Rajh, T.; Meyer, H. M., III; Paranthaman, M. P.; *et al.* Band Gap Narrowing of Titanium Oxide Semiconductors by Noncompensated Anion-Cation Codoping for Enhanced Visible-Light Photoactivity. *Phys. Rev. Lett.* **2009**, *103*, 226401.
52. Yang, K.; Dai, Y.; Huang, B.; Whangbo, M.-H. Density Functional Characterization of the Visible-Light Absorption in Substitutional C-Anion- and C-Cation-Doped TiO_2. *J. Phys. Chem. C* **2009**, *113*, 2624–2629.

53. Zhou, Z.; Li, M.; Guo, L. A First-Principles Theoretical Simulation on the Electronic Structures and Optical Absorption Properties for O Vacancy and Ni Impurity in TiO_2 Photocatalysts. *J. Phys. Chem. Solids* **2010**, *71*, 1707–1712.
54. Ma, X.; Wu, Y.; Lu, Y.; Xu, J.; Wang, Y.; Zhu, Y. Effect of Compensated Codoping on the Photoelectrochemical Properties of Anatase TiO_2 Photocatalyst. *J. Phys. Chem. C* **2011**, *115*, 16963–16969.
55. Pan, J.; Liu, G.; Lu, G. Q. M.; Cheng, H.-M. On the True Photoreactivity Order of {001}, {010}, and {101} Facets of Anatase TiO_2 Crystals. *Angew. Chem., Int. Ed.* **2011**, *50*, 2133–2137.
56. Pan, J.; Wu, X.; Wang, L.; Liu, G.; Lu, G. Q.; Cheng, H.-M. Synthesis of Anatase TiO_2 Rods with Dominant Reactive {010} Facets for the Photoreduction of CO_2 to CH_4 and Use in Dye-Sensitized Solar Cells. *Chem. Commun.* **2011**, *47*, 8361–8363.
57. Chen, X.; Shen, S.; Guo, L.; Mao, S. S. Semiconductor-Based Photocatalytic Hydrogen Generation. *Chem. Rev.* **2010**, *110*, 6503–6570.